Crystallization Temperature-Dependent Crystal Orientations within Nanoscale Confined Lamellae of a Self-Assembled Crystalline−Amorphous Diblock Copolymer

Lei Zhu,[†] Stephen Z. D. Cheng,*[,†] Bret H. Calhoun,[†] Qing Ge,[†] Roderic P. Quirk,[†] Edwin L. Thomas,[‡] Benjamin S. Hsiao,[§] Fengji Yeh,[§] and Bernard Lotz[⊥]

Contribution from the Maurice Morton Institute and Department of Polymer Science, The University of Akron, Akron, Ohio 44325-3909, Department of Materials Science and Engineering, Massachusetts Institute of Technology, Cambridge, Massachusetts, 02139, Department of Chemistry, The State University of New York at Stony Brook, Stony Brook, New York 11794-3400, and Institute Charles Sadron, 6 Rue Boussingault, Strasbourg 67083, France

Received January 25, 2000

Abstract: For a lamella-forming poly(ethylene oxide)-*block*-polystyrene (PEO-*b*-PS) diblock copolymer ($\bar{M}_n^{PEO}$ = 8.7K and $\bar{M}_n^{PS}$ = 9.2K), the glass transition temperature of the PS blocks is 62 °C, and the melting temperature of the PEO crystals is around 51 °C when the sample is crystallized below 40 °C. The PEO blocks thus crystallize in a one-dimensionally confined lamellar space of 8.8 nm, as studied recently by one-dimensional small-angle X-ray scattering (SAXS) and transmission electron microscopy. In this report, the crystal orientation (the *c*-axis of the PEO crystals) within nanoscale confined lamellae has been investigated using combined two-dimensional SAXS and wide-angle X-ray scattering experiments. The *c*-axis orientation in the PEO crystals is observed for the first time to change from random to perpendicular, then to inclined, and finally to parallel to the lamellar surface normal, depending only on the crystallization temperature (T_c). Detailed crystallographic analyses indicate that the *c*-axis orientation at each T_c corresponds to a uniform orientation rather than a mixture of different crystal orientations.

Introduction

During the past few decades, phase transformations within confined geometry have received substantial attention. It is well documented that various ordered phase morphologies, such as lamellae, double gyroid, cylinders, and spheres, have been found for diblock copolymers on a length scale of a few nanometers, as a consequence of microphase separation of the dissimilar components.[1] A convenient and effective way to construct well-defined and uniformly oriented nanoenvironments is to use diblock copolymers as templates. For example, confined liquid-crystal formation in nanoenvironments can be studied using liquid crystalline−amorphous diblock copolymers,[2] and confined polymer crystallization can be studied using crystalline−amorphous diblock copolymers.[3] Here, the amorphous blocks are usually vitrified to ensure the nanoconfinement.

In the present research, confined polymer crystallization has been studied using crystalline−amorphous diblock copolymers. Generally speaking, for low-molecular-weight crystalline−amorphous diblock copolymers, crystallization of crystallizable blocks can be efficiently confined within nanoenvironments when the amorphous blocks vitrify prior to the crystallization, i.e., the order−disorder transition temperature (T_{ODT}) > the glass transition temperature (T_g[a]) > the crystallization temperature (T_c).[4] Among the various phase morphologies of bulk block copolymers, the simplest is the lamellar morphology, which is one-dimensionally (1D) confined. For confined crystallization within the lamellar geometry, two extremes of chain orientations in chain-folded crystals with respect to the lamellar normal ($\hat{n}$) can be found. Namely, the chain direction (in most cases, the *c*-axis of crystals) is oriented either perpendicular (a homogeneous configuration) or parallel (a homeotropic configuration) to $\hat{n}$.

In the 1960s, polystyrene-sandwiched lamellar single crystals of poly(ethylene oxide)-*block*-polystyrene (PEO-*b*-PS) grown from dilute solution were studied using the electron diffraction (ED) technique. From the ED pattern of the single crystals, the chain direction in the crystals was found to be parallel to $\hat{n}$.[5−7] Later, in 1975, the homeotropic crystal orientation was found for poly(ethylene oxide)-*block*-polyisoprene block copolymers, as studied by combined two-dimensional (2D) small-angle X-ray scattering (SAXS) and wide-angle X-ray scattering (WAXS) on solution-cast block copolymer films.[8] Recently, this kind of

* To whom correspondence should be addressed. E-mail: cheng@polymer.uakron.edu.
[†] The University of Akron.
[‡] Massachusetts Institute of Technology.
[§] The State University of New York at Stony Brook.
[⊥] Institute Charles Sadron.

(1) Bates, F. S.; Fredrickson, G. H. *Annu. Rev. Phys. Chem.* **1990**, *41*, 525.
(2) Osuji, C. O.; Chen, J. T.; Mao, G.; Ober, C. K.; Thomas, E. L. *Polymer*, in press.
(3) Weimann, P. A.; Hajduk, D. A.; Chu, C.; Chaffin, K. A.; Brodil, J. C.; Bates, F. S. *J. Polym. Sci., Polym. Phys.* **1999**, *37*, 2053.
(4) Zhu, L.; Chen, Y.; Zhang, A.; Calhoun, B. H.; Chun, M.; Quirk, R. P.; Cheng, S. Z. D.; Hsiao, B. S.; Yeh, F.; Hashimoto, T. *Phys. Rev. B* **1999**, *60*, 10022.
(5) Lotz, B.; Kovacs, A. J. *Kolloid-Z. Z. Polym.* **1966**, *209*, 97.
(6) Lotz, B.; Kovacs, A. J.; Bassett, G. A.; Keller, A. *Kolloid-Z. Z. Polym.* **1966**, *209*, 115.
(7) Kovacs, A. J.; Lotz, B.; Keller, A. *J. Macromol. Sci. Phys.* **1969**, *B3* (3), 385.
(8) Hirata, E.; Ijitsu, T.; Hashimoto, T.; Kawai, H. *Polymer* **1975**, *16*, 249.

10.1021/ja000275e CCC: $19.00
Published on Web 06/06/2000

chain orientation in the crystals was also found for poly(ethylene oxide)-*block*-poly(butylene oxide) (PEO-*b*-PBO) diblock copolymers, based on SAXS and low-frequency Raman spectroscopy results.[9] The homeotropic crystal orientation has been used frequently to formulate theoretical approaches[10,1110,11] and explain experimental observations.[12−17] This configuration is speculated to possess the most thermodynamic stability.

In contrast, homogeneous crystal orientation was observed exclusively for shear-aligned polyethylene (PE)-containing block copolymers having microphase-separated lamellar morphology based on WAXS pole figure analysis[18,19] and 2D WAXS experiments.[20−22] It was speculated that this unusual crystal orientation may be facilitated by the intermaterial dividing surfaces[19] and is probably caused by the high molecular weights in the PE blocks.[21,22]

In other cases, a tilted crystal orientation with respect to $\hat{n}$ was also proposed for PEO-*b*-PBO[23,2423,24] and PE-*b*-PEO[25] diblock copolymers. Since the molecular weights in the crystallizable blocks are low, extended chain conformation in the crystals is assumed. Based on the SAXS results, the polymer chains are calculated to tilt around 30−40° away from $\hat{n}$ in order to fit the lamellar thickness.

In our recent study,[26] a PEO-*b*-PS (8.7K−9.2K) diblock copolymer has been chosen as a model system to study confined polymer crystallization within nanoscale lamellae. Differential scanning calorimetry results show that the glass transition temperature of the PS blocks (T_g^{PS}) and the melting temperature of the PEO blocks (T_m^{PEO}) are determined to be 62 and ∼51 °C (for T_c < 40 °C), respectively. It has been found that between two glassy PS layers, PEO blocks crystallize in a confined lamellar space of 8.8 nm based on 1D SAXS and transmission electron microscopy observations. The T_{ODT} is determined to be 160 °C by temperature-dependent 1D SAXS. Confined crystallization kinetics and crystallinity of the PEO blocks between the glassy PS layers has also been followed by time-resolved simultaneous 1D SAXS and WAXS experiments.[26] In this report, crystal orientation within the confined lamellae is investigated by combined 2D SAXS and WAXS on shear-aligned PEO-*b*-PS samples, and various crystal orientations are obtained by varying only the T_c.

Experimental Section

Materials and Sample Preparation. The PEO-*b*-PS diblock copolymer was synthesized via sequential anionic block copolymerization of styrene and ethylene oxide. Detailed synthesis procedures can be found elsewhere.[26,27] The PS precursor was characterized by size exclusion chromatography (SEC) using polystyrene standard and had an $\bar{M}_n$ of 9.2K and a polydispersity of 1.02. The $\bar{M}_n$ of the PEO blocks was determined by proton nuclear magnetic resonance (^{1}H NMR) to be 8.7K, and the polydispersity of 1.04 in the final diblock copolymer was determined by SEC using universal calibration. The volume fraction of PEO blocks is thus 0.473 in the melt at 60 °C (the densities of amorphous PEO and PS are 1.092 and 1.035 g/cm^3).[26]

To ensure the consistency of the phase behavior, uniform sample preparation procedure and thermal history were necessary. The sample was cast from a 5% (w/v) toluene solution, and the solvent was allowed to evaporate slowly under a dry nitrogen atmosphere at 50 °C to prevent the crystallization of the PEO blocks. Residual solvent was removed under vacuum at 50 °C for 1 day, and the sample was then annealed at 95 °C for 12 h to allow the development of microphase separation. To study the crystal orientation in this copolymer, the microphase-separated samples were subjected to large-amplitude oscillating shear (LAOS) under a dry argon atmosphere at 110 °C to achieve uniform, parallel alignment of the lamellar phase morphology. The shear frequency was 0.5 Hz, and the shear amplitude was 150%. The shear-aligned samples were further annealed at 95 °C for another 12 h in a vacuum oven to eliminate any residual stresses.

Equipment and Experiments. Simultaneous 2D SAXS and WAXS experiments were conducted at the synchrotron X-ray beamline X27C at the National Synchrotron Light Source in Brookhaven National Laboratory. The wavelength of the X-ray beam was 0.1307 nm. The zero pixel of the 2D SAXS pattern was calibrated using silver behenate, with the first-order scattering vector q^* ($q^* = 4\pi \sin\theta/\lambda$, where λ is the wavelength and 2θ the scattering angle) being 1.076 nm^{-1}. 2D WAXS were calibrated using α-Al_2O_3 with known crystal diffractions, and air scattering is subtracted. Conventional 2D WAXS experiments were conducted on Rigaku 18 kW rotating anode generator equipped with an image plate as the detector, and the detector was calibrated using silicon powders with 2θ being 28.4° under Cu Kα radiation. The air scattering is also subtracted. The same samples were used in both synchrotron and conventional WAXS experiments. Azimuthal profiles for 2D WAXS patterns were obtained via scans, which started on the vertical direction of the patterns. The standard deviation of determining the angular maxim is ±3°.

Isothermal crystallization experiments were conducted using an Instec LN2-P2 hot stage equipped with a liquid nitrogen cooling system. The isothermal T_c was controlled to within ±0.1 °C. The shear-aligned samples were preheated to 70 °C for 3 min and then quickly quenched (switched) to the hot stage at a preset T_c for crystallization.

Results and Discussion

Structure of PEO Crystals and Its Diffraction Behavior. Linear PEO has two crystalline forms. One form has a helical conformation (monoclinic),[28,2928,29] and the other has a planar-zigzag conformation (triclinic).[30] The monoclinic lattice is commonly observed in PEO crystals, and the crystal having the planar-zigzag conformation can only be seen under large deformation. In this study, the PEO blocks are found to crystallize into the monoclinic form.

The monoclinic unit cell of PEO crystals is defined by parameters a = 0.805 nm, b = 1.304 nm, c = 1.948 nm, and β = 125.4°.[29] The space group is $P2_1/a$-C_{2h}^5, which is determined by the systematic absences of $h0l$ when h is odd and

(9) Yang, Y.-W.; Tanodekaew, S.; Mai, S.-M.; Booth, C.; Ryan, A. J.; Bras, W.; Viras, K. *Macromolecules* **1995**, *28*, 6029.
(10) DiMarzio, E. A.; Guttman, C. M.; Hoffman, J. D. *Macromolecules* **1980**, *13*, 1194.
(11) Whitmore, M. D.; Noolandi, J. *Macromolecules* **1988**, *21*, 1482.
(12) Rangarajan, P.; Register, R. A.; Adamson, D. H.; Fetters, L. J.; Bras, W.; Naylor, S.; Ryan, A. J. *Macromolecules* **1995**, *28*, 1422.
(13) Rangarajan, P.; Register, R. A.; Fetters, L. J. *Macromolecules* **1993**, *26*, 4640.
(14) Vilgis, T.; Halperin, A. *Macromolecules* **1991**, *24*, 2090.
(15) Crystal, R. G.; O'Malley, J. J.; Erhardt, P. F. *Polym. Prepr., Am. Chem. Soc., Div. Polym. Chem.* **1969**, *10* (2), 804.
(16) Rangarajan, P.; Register, R. A.; Fetters, L. J. *Macromolecules* **1993**, *26*, 4640.
(17) Gervais, M.; Gallot, B. *Makromol. Chem.* **1977**, *178*, 1577.
(18) Douzinas, K. C.; Cohen, R. E. *Macromolecules* **1992**, *25*, 5030.
(19) Cohen, R. E.; Bellare, A.; Drzewinski, M. A. *Macromolecules* **1994**, *27*, 2321.
(20) Séguéla, R.; Prud'homme, J. *Polymer* **1989**, *30*, 1446.
(21) Hamley, I. W.; Fairclough, J. P. A.; Ryan, A. J.; Bates, F. S.; Towns-Andrews, E. *Polymer* **1996**, *37*, 4425.
(22) Hamley, I. W.; Fairclough, J. P. A.; Terrill, N. J.; Ryan, A. J.; Lipic, P. M.; Bates, F. S.; Towns-Andrews, E. *Macromolecules* **1996**, *29*, 8835.
(23) Viras, F.; Luo, Y.-Z.; Viras, K.; Mobbs, R. H.; King, T. A.; Booth, C. *Makromol. Chem.* **1988**, *189*, 459.
(24) Hamley, I. W.; Wallwork, M. L.; Smith, D. A.; Fairclough, J. P. A.; Ryan, A. J.; Mai, S.-M.; Yang, Y. W.; Booth, C. *Polymer* **1998**, *39*, 3321.
(25) Hillmyer, M. A.; Bates, F. S. *Macromol. Symp.* **1997**, *117*, 121.
(26) Zhu, L. Ph.D. Dissertation, Department of Polymer Science, The University of Akron, 2000.
(27) Quirk, R. P.; Kim, J.; Kausch, C.; Chun, M. S. *Polym. Int.* **1996**, *39*, 3.
(28) Tadokoro, H.; Chatani, Y.; Yoshihara, T.; Tahara, S.; Murahashi, S. *Makromol. Chem.* **1964**, *73*, 109.
(29) Takahashi, Y.; Tadokoro, H. *Macromolecules* **1973**, *6*, 672.
(30) Takahashi, Y.; Sumita, I.; Tadokoro, H. *J. Polym. Sci., Polym. Phys. Ed.* **1973**, *11*, 2113.

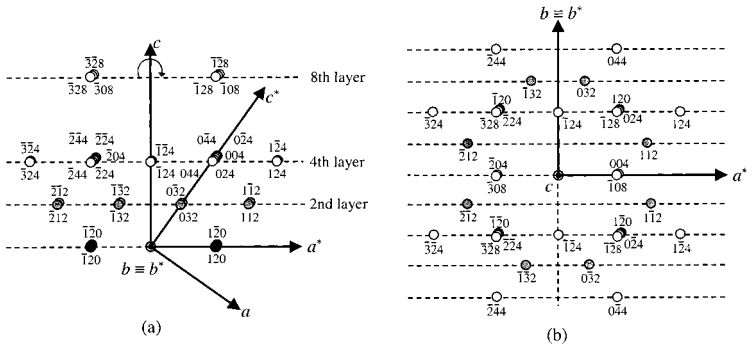

Figure 1. Different reflections in the PEO crystal reciprocal lattice: (a) viewed through the *b*-axis with the *c*-axis vertical; (b) viewed through the *c*-axis with the *b*-axis vertical.

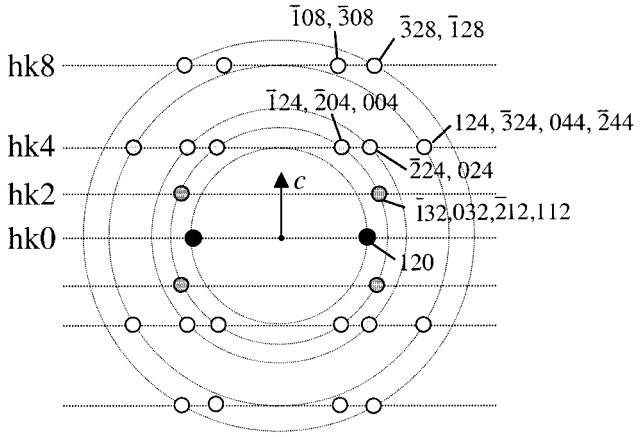

Figure 2. Fiber pattern of PEO crystals constructed by rotating the reciprocal lattice along the *c*-axis.

*0k*0 when *k* is odd. In one unit cell, four helical molecules pass through along the *c*-axis, which is nearly perpendicular to the $(10\bar{4})$ plane.[31,3231,32] The helix has a 7/2 conformation, which is distorted from a D_7 point group due to the flexibility of PEO chains and intermolecular interactions. The helical conformation corresponds closely to a *gauche*−*trans*−*trans* sequence of bond rotations, at which the gauche conformation is between the two CH_2 groups.

Based on the monoclinic PEO crystal structure, various reflections in the reciprocal space as viewed through both the *b*- and *c*-axes are shown in Figure 1a and b, respectively. The reciprocal space coordinates for the PEO crystals are $a^* = 1/(a \sin\beta) = 1.524\ \text{nm}^{-1}$, $b^* = 1/b = 0.767\ \text{nm}^{-1}$, $c^* = 1/(c \sin\beta) = 0.630\ \text{nm}^{-1}$, and $\beta^* = 180° - \beta = 54.6°$. If all the reflections rotate around the *c*-axis, a PEO crystal fiber pattern can be obtained, as shown in Figure 2, which is consistent with the experimental WAXS fiber pattern.[28,29] The *d*-spacings for each set of reflections and the angles between each set of reflections and the *c*-axis are listed in Table 1.

2D SAXS and WAXS Analyses for Shear-Aligned Samples. The shear geometry is shown in Figure 3. The shear direction is along $\hat{x}$, and the vorticity direction is along $\hat{z}$. After the LAOS the parallel lamellar morphology is obtained. The lamellar geometry is defined as $\hat{n} \parallel \hat{z}$ and $\hat{n} \perp$ the $\hat{x}$−$\hat{y}$ plane. Figure 3 also shows 2D SAXS and WAXS results on a shear-aligned sample when the X-ray beam is along $\hat{x}$, $\hat{y}$, and $\hat{z}$, respectively, when the sample is isothermally crystallized at −10 °C. From the SAXS results, the patterns obtained when the X-ray beams

Table 1. *d*-Spacings and Angles between Each Set of Reflections and the *c*-Axis in PEO Crystals

reflections	*d*-spacing (nm)	angles with respect to the *c*-axis (deg)
120	0.463	90.0
032	0.381	67.0
$\bar{1}32$	0.379	67.1
112	0.386	66.7
$\bar{2}12$	0.378	67.2
$\bar{2}04$	0.385	37.7
004	0.397	35.4
$\bar{1}24$	0.390	36.8
$\bar{2}24$	0.339	47.1
024	0.332	45.9
124	0.254	58.5
$\bar{3}24$	0.248	59.4
044	0.252	58.8
$\bar{2}44$	0.249	59.3
$\bar{1}08$	0.231	18.8
$\bar{3}08$	0.226	21.9
$\bar{3}28$	0.213	28.8
$\bar{1}28$	0.217	26.8

are along $\hat{x}$ (Figure 3a) and $\hat{y}$ (Figure 3b) are practically identical. Up to four orders of scattering peaks can be observed on $\hat{z}$, and $q/q^* = 1{:}2{:}3{:}4$. At the same time, there is no discernible diffraction in the 2D SAXS when the X-ray beam is along $\hat{z}$ (Figure 3c). These results indicate that the block copolymer lamellae are macroscopically aligned parallel to the $\hat{x}$−$\hat{y}$ plane. The vertical streaks in Figure 3a,b may originate from microdefects (such as voids etc.) in the shear-aligned sample. The corresponding 2D WAXS along $\hat{x}$, $\hat{y}$, and $\hat{z}$ are shown in Figure 3d, e, and f. The 2D WAXS patterns obtained along both $\hat{x}$ and $\hat{y}$ are the same, while that along $\hat{z}$ is different, indicating that the PEO crystal orientation is identical in both $\hat{x}$ and $\hat{y}$, and the orientation is random along $\hat{z}$. This phenomenon can also be observed for the samples isothermally crystallized at different T_cs, in which the 2D SAXS and WAXS patterns along both $\hat{x}$ and $\hat{y}$ are identical. Therefore, only the diffractions along $\hat{y}$ are used for the following discussion.

Crystal Orientation When Quenched into Liquid Nitrogen from the Melt. The shear-aligned sample is heated and held at 70 °C for 3 min in order to completely melt the PEO crystals and then quickly quenched into liquid nitrogen. 2D SAXS and WAXS along $\hat{y}$ are shown in Figure 4a,b, and 2D SAXS and WAXS along $\hat{z}$ are shown in Figure 4c,d. In Figure 4a, multiple orders of 2D SAXS can be clearly observed along $\hat{z}$. No discernible SAXS in Figure 4c is found. These patterns are identical to those in Figure 3b,c. Both parts b and d of Figure 4 show isotropic (ring) reflections in 2D WAXS, indicating a random crystal orientation within the confined lamellae. These results also suggest little postshear effect on the crystallization

(31) Balta Calleja, F. B.; Hay, I. L.; Keller, A. *Kolloid-Z. Z. Polym.* **1967**, *209*, 128.
(32) Chen, J.; Cheng, S. Z. D.; Wu, S. S.; Lotz, B.; Wittmann, J.-C. *J. Polym. Sci. Polym. Phys. Ed.* **1995**, *33*, 1851.

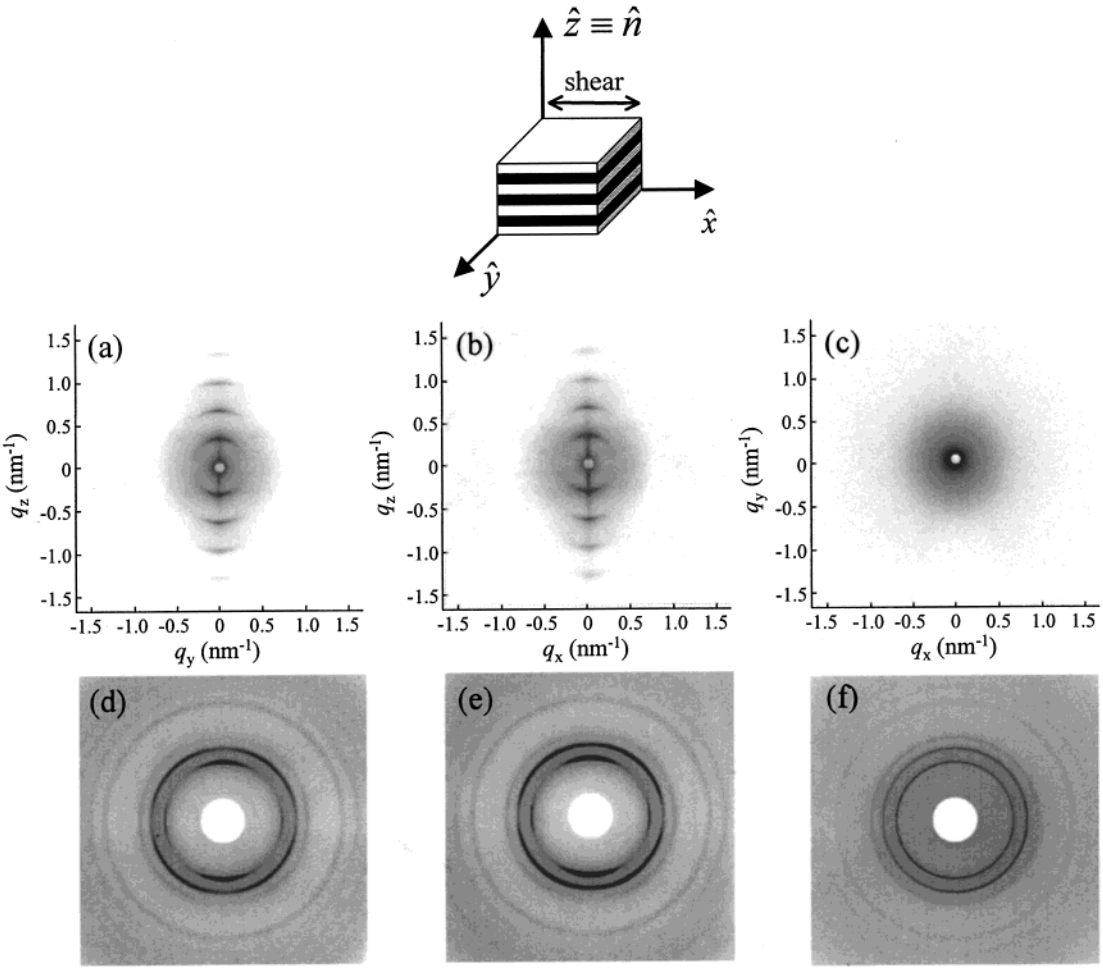

Figure 3. X-ray scattering patterns of shear-aligned PEO-*b*-PS (8.7K-9.2K) sample isothermally crystallized at −10 °C. The sheared lamellar geometry is shown on the top. (a) 2D SAXS obtained when the X-ray beam is parallel to $\hat{x}$; (b) 2D SAXS along $\hat{y}$; (c) 2D SAXS along $\hat{z}$; (d) 2D WAXS along $\hat{x}$; (e) 2D WAXS along $\hat{y}$; and (f) 2D WAXS along $\hat{z}$.

of the PEO blocks. A real-space model is illustrated in Figure 4e. During this liquid nitrogen quenching process, a large number of nucleation sites are created. It is speculated that the nucleation density is so high that little crystal growth is needed to complete crystallization. In other words, the randomly oriented PEO crystals are too small to "*feel*" the 1D confinement provided by the glassy PS layers.

Crystal Orientation When Isothermally Crystallized between $-50 \le T_c \le -10$ °C. The 2D SAXS and WAXS patterns along $\hat{y}$ and $\hat{z}$ obtained after the sample is quickly quenched from the melt to temperatures between −50 and −10 °C are shown in Figure 5a−d. The 2D SAXS patterns in Figure 5a,c are the same as those previously described in Figures 3 and 4, indicating again that the crystallization of the PEO blocks is completely confined in the 1D lamellae, and the lamellar phase morphology is preserved after the crystallization. Since the 2D WAXS patterns along $\hat{z}$ in Figure 5d are isotropic, the *c*-axis of PEO crystals is macroscopically isotropic with respect to $\hat{n}$. However, the 2D WAXS patterns obtained along $\hat{y}$ in Figure 5b give clear oriented (120) reflections (*d*-spacing of 0.463 nm) with major intensity along $\hat{z}$, and minor intensity in the $\hat{x}-\hat{y}$ plane. The overlapped reflections on the second reflection ring (*d*-spacing of 0.38−0.40 nm) of the 2D WAXS patterns are oriented in the quadrants.

This diffraction pattern can be quantitatively explained using a [120] uniaxial pattern, with [120] $\equiv \hat{z}$ (or $\hat{n}$). Different reflections of PEO crystals in the reciprocal space viewed through [120] (see Figure 1b) are shown in Figure 6a. A rotation around [120] generates a [120] uniaxial pattern, as shown in Figure 6b. The angles between different reflections and the [120] direction are listed in Table 2.

Based on this [120] uniaxial pattern (Figure 6b), there should be four (120) reflections on the first reflection ring (*d*-spacing of 0.463 nm), with the intensities on the meridian much stronger than those on the equator. The azimuthal profiles of the experimental (120) reflections obtained in 2D WAXS patterns along $\hat{y}$ (Figure 5b) at different T_cs are shown in Figure 7a. With increasing T_c, the orientation of the (120) reflections progressively improves. At $T_c = -10$ °C, it is clear that two sets of the (120) reflections are 90° apart from each other, with one set at $\phi = 0°$ and 180° stronger and the other at $\phi = 90°$ and 270° much weaker. This is consistent with the predicted [120] uniaxial diffraction pattern.

In the predicted [120] uniaxial diffraction pattern (Figure 6b), eight reflections on the second reflection ring (*d*-spacing of 0.38−0.40 nm) are attributed to the overlapped $(\bar{1}32)$, (032), (112), $(\bar{2}12)$, $(\bar{1}24)$, $(\bar{2}04)$, and (004) reflections at $\phi = 35°$, 65°, 115°, 145°, 215°, 245°, 295°, and 325°. The azimuthal profiles of this ring in the 2D WAXS patterns along $\hat{y}$ (Figure 5b) at different T_cs are shown in Figure 7b. It can be recognized that the orientation of the overlapped reflections is also enhanced with increasing T_c. At $T_c = -10$ °C, eight reflections are found at $\phi = 33°$, 64°, 116°, 147°, 213°, 244°, 298°, and 327°, respectively, which fit well to the diffraction pattern predicted

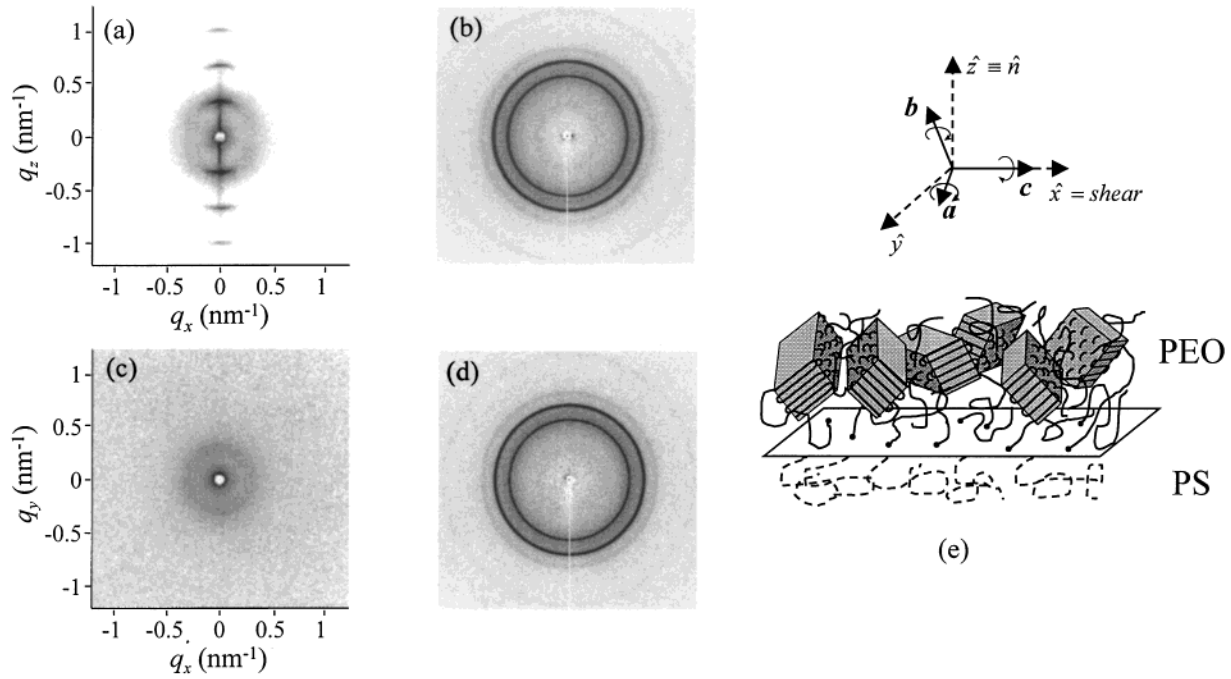

Figure 4. X-ray scattering patterns of shear-aligned PEO-*b*-PS (8.7K−9.2K) sample quickly quenched into liquid nitrogen. (a) 2D SAXS obtained when the X-ray beam is parallel to $\hat{y}$; (b) 2D WAXS along $\hat{y}$; (c) 2D SAXS along $\hat{z}$; (d) 2D WAXS along $\hat{z}$; and (e) schematic of random crystal orientation within the confined lamella.

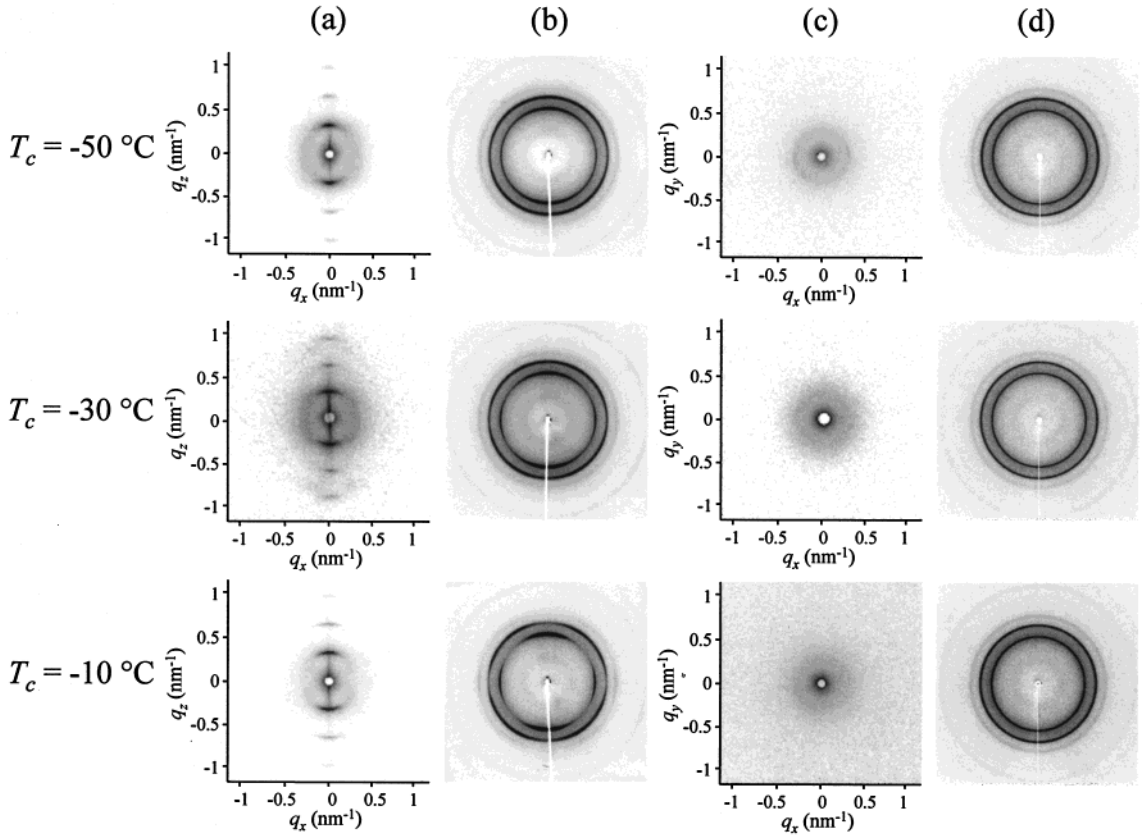

Figure 5. X-ray scattering patterns of shear-aligned PEO-*b*-PS (8.7K−9.2K) sample isothermally crystallized at −50, −30, and −10 °C. (a) 2D SAXS along $\hat{y}$; (b) 2D WAXS along $\hat{y}$; (c) 2D SAXS along $\hat{z}$; and (d) 2D WAXS along $\hat{z}$.

in Figure 6b. Slight misalignment of the [120] axis around the $\hat{z}$ direction (within the $\hat{x}-\hat{z}$ plane) may cause intensity changes in addition to the contributions of individual structural factors in these overlapped reflections.

Figure 6b also predicts that six reflections are on the third reflection ring (*d*-spacing of 0.33−0.34 nm), which are attributed to the overlapped (024) and ($\bar{2}$24) reflections at $\phi = 44°$, 90°, 136°, 224°, 270°, and 316°. The azimuthal profiles of this ring in the 2D WAXS patterns along $\hat{y}$ in Figure 5b are shown in Figure 7c. Again, with increasing T_c, the orientation becomes increasingly improved. At $T_c = -10$ °C, there are six maxima at $\phi = 40°$, 90°, 145°, 219°, 270°, and 323°, which fit well

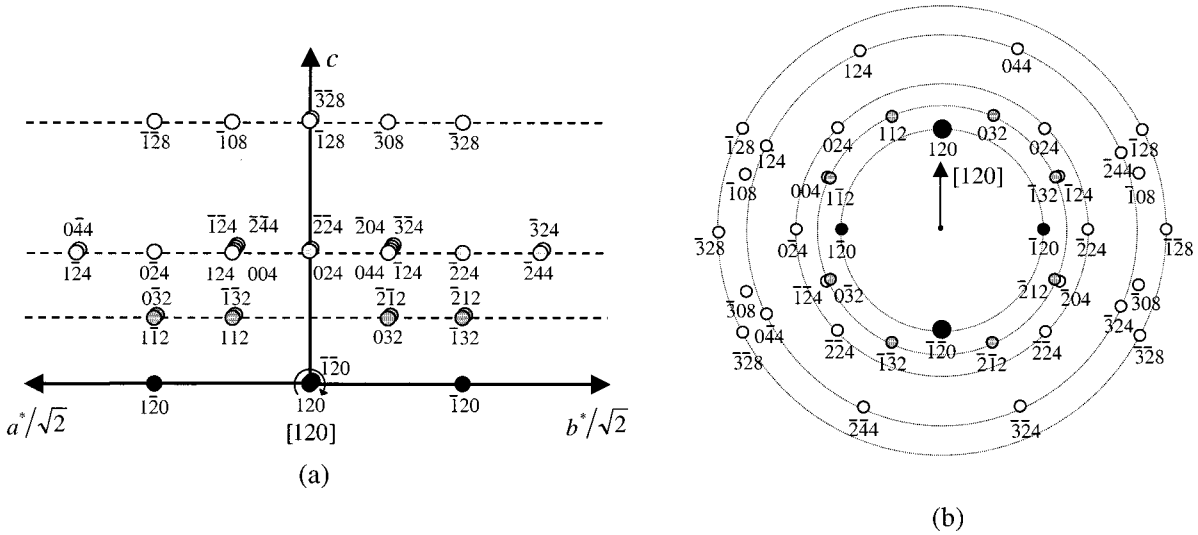

Figure 6. Different reflections in the PEO reciprocal lattice: (a) viewed through the [120] with the *c*-axis vertical; (b) the PEO [120] uniaxial pattern.

Table 2. Angles between Different Reflections and [120]

d-spacing (nm)	reflections	angles between different reflections and [120] (deg)
0.463	120 and $\bar{1}\bar{2}0$	0
(first ring)	$\bar{1}20$ and $1\bar{2}0$	90
0.38−0.40	032 and $\bar{1}\bar{3}2$	35.1
(second ring)	112 and $\bar{2}\bar{1}2$	34.7
	$\bar{1}32$ and $0\bar{3}2$	65.0
	$1\bar{1}2$ and $\bar{2}12$	66.3
	004	67.0
	$\bar{2}04$	64.5
	124 and $\bar{1}\bar{2}4$	66.0
0.33−0.43	024 and $0\bar{2}4$	44.1
(third ring)	$\bar{2}24$ and $\bar{2}\bar{2}4$	42.9
0.25	124 and $\bar{3}\bar{2}4$	35.8
(fourth ring)	044 and $\bar{2}44$	36.2
	$1\bar{2}4$ and $\bar{3}24$	75.0
	$\bar{2}24$ and $0\bar{4}4$	74.8
0.23[a]	$\bar{1}08$	81.0
	$\bar{3}08$	79.3
0.21−0.22	$\bar{3}28$ and $\bar{3}\bar{2}8$	61.2
(fifth ring)	$\bar{1}28$ and $1\bar{2}8$	63.2

[a] These reflections are very close to the fourth ring and, therefore, we do not count them as a separate ring.

with the predicted [120] uniaxial pattern (Figure 6b). The nonequal intensity of those reflections may be due to the slight misalignment of the [120] axis around $\hat{z}$.

Although the first three reflection rings of the WAXS pattern at $T_c = -10$ °C correspond well with the predicted [120] uniaxial pattern, another possibility for explaining the 2D WAXS patterns in Figure 5b exists: these 2D WAXS patterns may be constructed by mixtures of the [120] uniaxial patterns (Figure 6b) and the fiber pattern (Figure 2). This is because the above reflections discussed in Figure 7a−c can also be found in the fiber pattern. To determine that the observed WAXS patterns in Figure 5b are due to a single population of the crystal orientation, we need to find a reflection in the fiber pattern (Figure 2) that is not seen experimentally in Figure 5b. This can be fulfilled by analyzing the reflections on the fifth ring [the ($\bar{1}28$) and ($\bar{3}28$)] (*d*-spacing of 0.21−0.22 nm). These two reflections are located at $\phi = 62°$, 90°, 118°, 242°, 270°, and 298° in the predicted [120] uniaxial pattern (Figure 6b), while they are located at $\phi = 28°$, 152°, 208°, and 332° in the fiber pattern (Figure 2). From the 2D WAXS pattern along $\hat{y}$ at $T_c = -10$ °C (see Figure 3d instead of Figure 5b, because the fifth reflection ring is not included in Figure 5b), no distinct reflections at $\phi = 28°$, 152°, 208°, and 332° can be found. A quantitative result of the azimuthal profile of the ($\bar{1}28$) and ($\bar{3}28$) reflections obtained from Figure 3d is shown in Figure 7d, with two broad scattering peaks centered at 90° and 270°. It can be deconvoluted using six Gaussian functions, among which the peaks at 90° and 270° have double intensity (see Figure 6b). At $T_c = -10$ °C, therefore, the experimental 2D WAXS pattern does not provide any evidence for the existence of a mixture of the [120] uniaxial pattern and the fiber pattern. This implies that the *c*-axis of the PEO crystals is oriented perpendicular to $\hat{n}$ (the homogeneous configuration).

Based on the above analyses, a real-space representation of the crystal orientation between $-50 \le T_c \le -10$ °C is shown in Figure 8. Assuming that the *c*-axis of the PEO unit cell is perpendicular to $\hat{z}$ ($\hat{n}$) and randomly distributed in the $\hat{x}-\hat{y}$ plane, isotropic distributions of the (120) and the overlapped ($\bar{1}32$), (032), (112), ($\bar{2}12$), ($\bar{1}24$), ($\bar{2}04$), and (004) reflections are thus expected in the 2D WAXS pattern along $\hat{z}$ (Figure 5d). Since one set of (120) reflections is in the $\hat{x}-\hat{y}$ plane, as shown in Figure 5b, the [120] must be the fastest crystal growth direction in the melt crystallization, as previously speculated.[32,33] Therefore, the *b*-axis of the PEO unit cell tilts 45° from $\hat{z}$ (Figure 8). When the X-ray beam is parallel to $\hat{y}$, the crystal orientation exemplified by the left three crystals in Figure 8 gives rise to a pair of the (120) reflections on $\hat{z}$, but not in the $\hat{x}-\hat{y}$ plane. Only the fourth crystal on the far right of Figure 8 provides equal reflections both on $\hat{z}$ and in the $\hat{x}-\hat{y}$ plane. Since the population of PEO crystals on the far right is less than that of the rest, the intensity in the $\hat{x}-\hat{y}$ plane is thus weaker than that on $\hat{z}$.

Crystal Orientation When Isothermally Crystallized between $-5 \le T_c \le 30$ °C. When the shear-aligned sample is crystallized at T_c between −5 and 30 °C, the 2D SAXS and WAXS patterns along $\hat{y}$ and $\hat{z}$ are shown in Figure 9a−d. The 2D SAXS patterns in Figure 9a,c are again identical to those in Figure 5a,c, indicating that the lamellar phase morphology is preserved after the PEO crystallization. The 2D WAXS patterns along $\hat{z}$ are isotropic (Figure 9d), indicating the isotropic *c*-axis orientation in the PEO crystals with respect to $\hat{n}$. In the 2D

(33) Kovacs, A. J.; Straupe, C.; Gonthier, A. *J. Polym. Sci. Polym. Symp.* **1977**, *59*, 31.

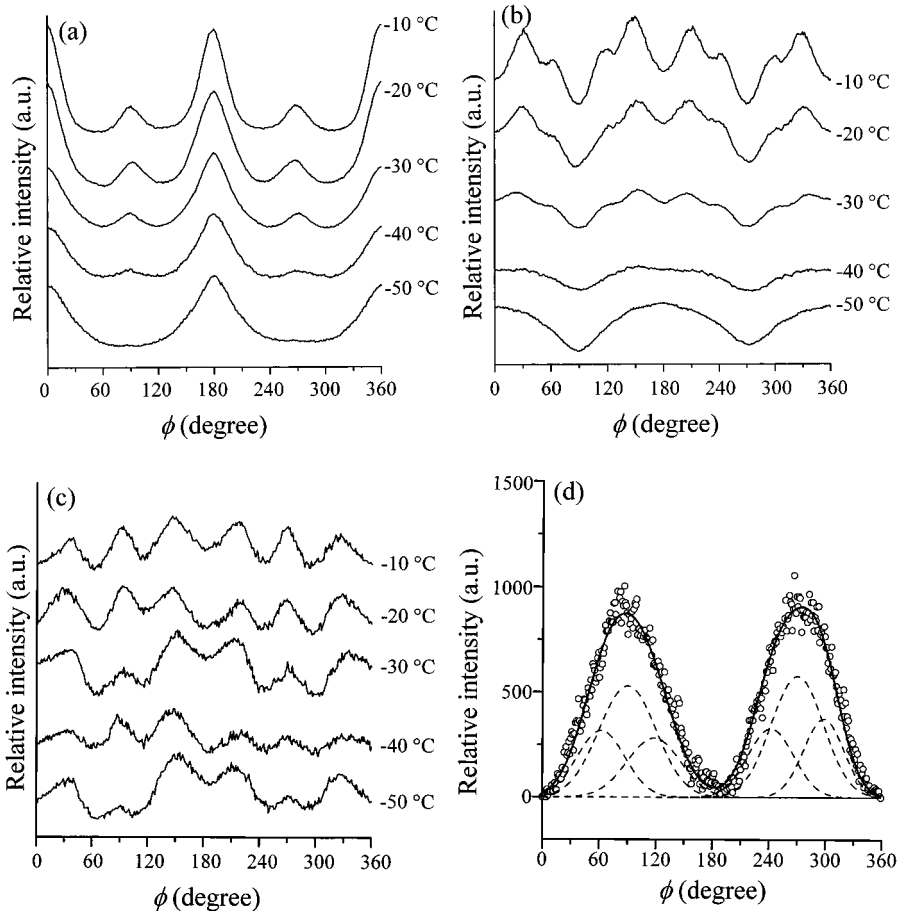

Figure 7. Azimuthal profiles for the PEO-*b*-PS (8.7K−9.2K) sample isothermally crystallized between $-50 \leq T_c \leq -10$ °C. (a) Azimuthal profiles of the (120) reflections on the first ring; (b) azimuthal profiles of the ($\bar{1}32$), (032), ($\bar{2}12$), (112), ($\bar{1}24$), ($\bar{2}04$), and (004) reflections on the second ring; (c) azimuthal profiles of the ($\bar{2}24$) and (024) reflections on the third ring; and (d) azimuthal profile of the ($\bar{3}28$) and ($\bar{1}28$) reflections on the fifth ring. The solid line is the best fit of the experimental data, and it can be deconvoluted into six Gaussian functions (dash line).

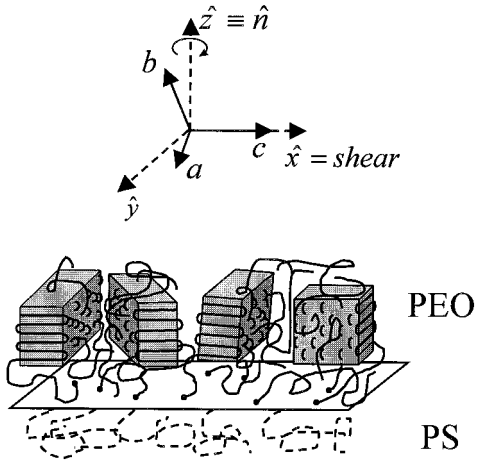

Figure 8. Schematic of a homogeneous crystal orientation within the confined lamella.

WAXS patterns along $\hat{y}$, the (120) reflections are located in both the quadrants and the $\hat{x}-\hat{y}$ plane, while those on $\hat{z}$ vanish with increasing T_c.

These diffraction patterns indicate a tilt crystal orientation with respect to $\hat{n}$, and the tilt angle of the crystal *c*-axis away from the lamellar surface gradually increases with increasing T_c. To quantitatively analyze the diffraction patterns with the tilted *c*-axis orientation, we construct a 45°-tilted reciprocal lattice for PEO crystals as an example (Figure 10a). If we rotate the reciprocal lattice around the 45° tilt axis ($\hat{n}_{45°}$) with one set of the (120) reflections always perpendicular to $\hat{n}_{45°}$, the corresponding uniaxial pattern can be obtained (Figure 10b). It should be noted that the reflections with $+l$ and $-l$ are no longer symmetric with respect to the $\hat{x}-\hat{y}$ plane. The total number of reflections in the $\hat{n}_{45°}$ uniaxial pattern is thus doubled compared with that in the [120] uniaxial pattern. The angles between the different reflections and the $\hat{n}_{45°}$ direction are listed in Table 3.

The tilt angle of the *c*-axis from the $\hat{x}-\hat{y}$ plane is observed to be 45° when $T_c = 0$ °C, and hence, the 2D WAXS pattern obtained along $\hat{y}$ (Figure 11a) can be compared to the predicted $\hat{n}_{45°}$ uniaxial pattern. As shown in Figure 10b, there are six (120) reflections on the first ring (*d*-spacing of 0.463 nm) at $\phi = 45°$, 90°, 135°, 225°, 270°, and 315°. The azimuthal profiles for these experimental (120) reflections at different T_cs are shown in Figure 11b. For the 2D WAXS pattern at $T_c = 0$ °C, six maxima at 42°, 90°, 133°, 223°, 270°, and 313° are consistent with the predicted $\hat{n}_{45°}$ uniaxial pattern. In Figure 11b, the six maxima gradually merge with increasing T_c, revealing the increase of the tilt angle away from the $\hat{x}-\hat{y}$ plane with increasing T_c. In Figure 10b, there are reflections on the second reflection ring (*d*-spacing of 0.38−0.40 nm) at $\phi = 30°$, 60°, 75°, 85°, 100°, 105°, 120°, 150°, 210°, 240°, 255°, 265°, 280°, 285°, 300°, and 330° (the assignments of the reflections can be found in Table 3). The azimuthal profiles of the reflections on the second ring for different T_cs are shown in Figure 11c. For the experimental 2D WAXS pattern at $T_c = 0$ °C, there are eight maxima observed with $\phi = 28°$, 73°, 107°, 154°, 202°, 253°, 286°, and 335°. Note that the reflections around 60°, 75°, and 85° in Figure

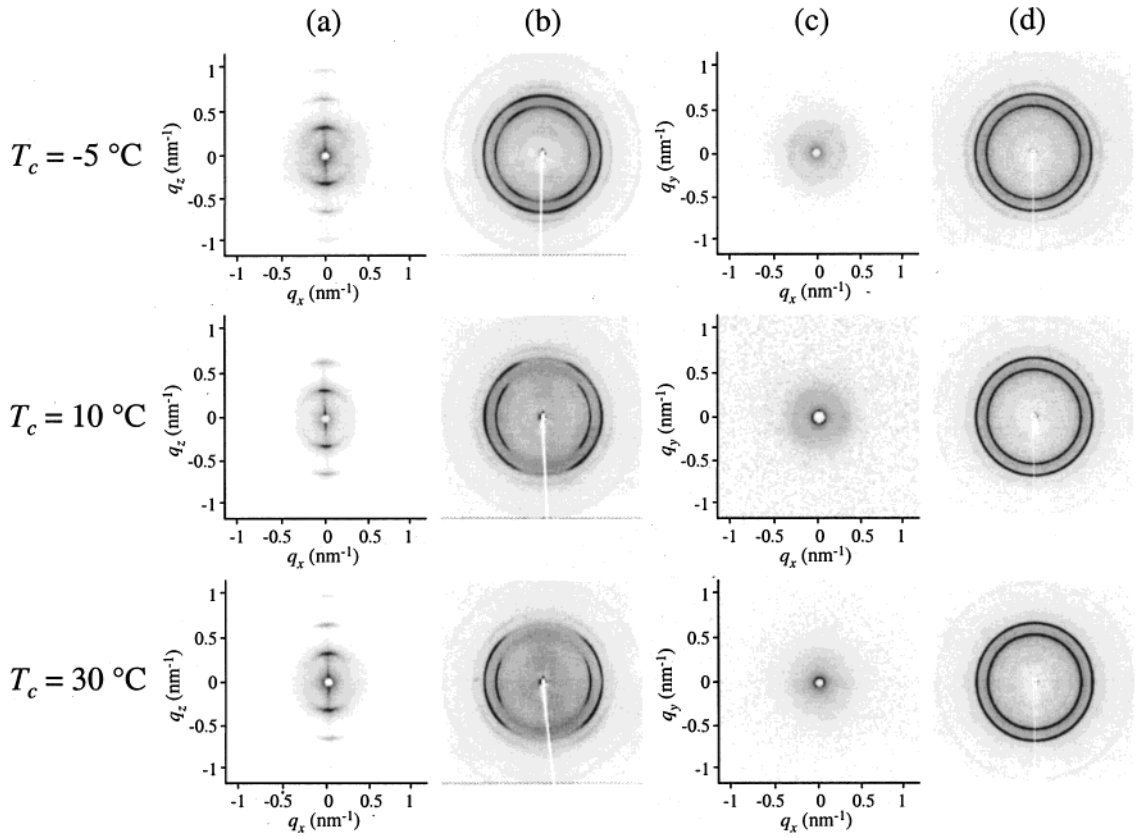

Figure 9. X-ray scattering patterns of the shear-aligned PEO-*b*-PS (8.7K−9.2K) sample isothermally crystallized at −5, 10, and 30 °C. (a) 2D SAXS along $\hat{y}$; (b) 2D WAXS along $\hat{y}$; (c) 2D SAXS along $\hat{z}$; and (d) 2D WAXS along $\hat{z}$.

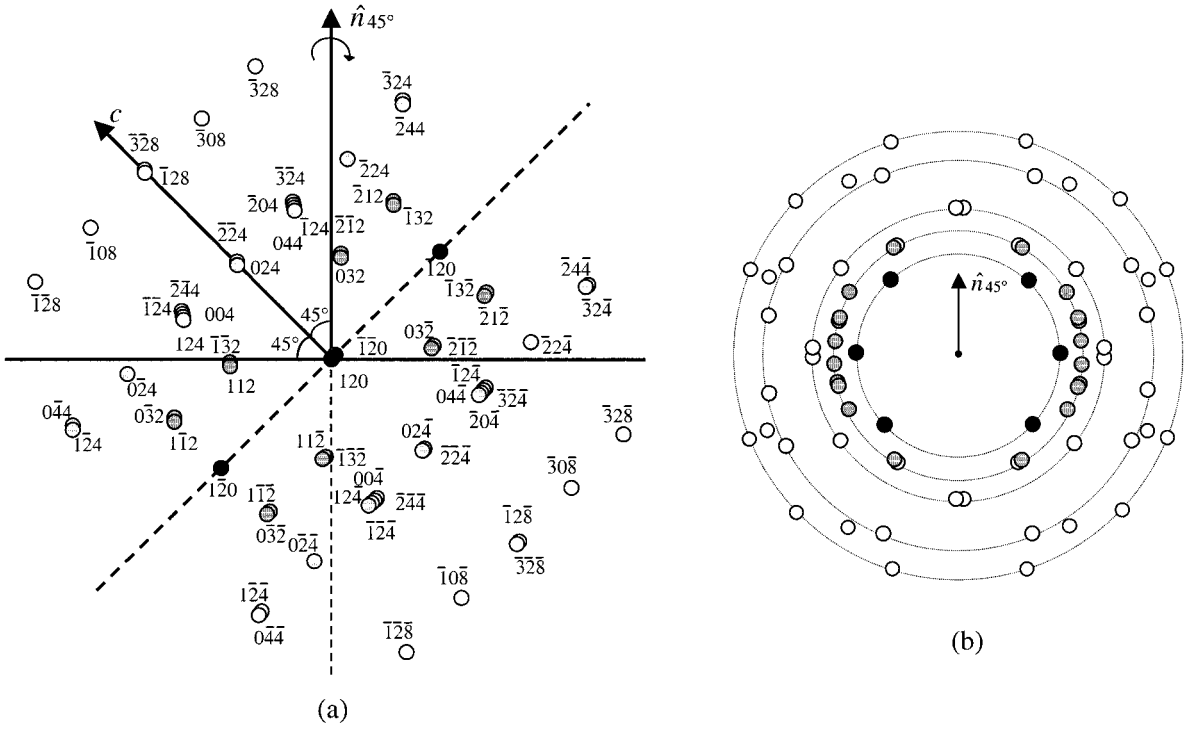

Figure 10. (a) Different reflections in the PEO reciprocal lattice viewed through the [120] with the *c*-axis tilt 45° to the left (or the $\hat{n}_{45°}$ vertical); (b) the PEO $\hat{n}_{45°}$ uniaxial pattern. The (120) reflections are on the first ring. The ($\bar{1}$32), (032), ($\bar{2}$12), (112), ($\bar{1}$24), ($\bar{2}$04), and (004) reflections are on the second ring. The ($\bar{2}\bar{2}$4) and (024) reflections are on the third ring. The (124), ($\bar{3}$24), (044), ($\bar{2}$44), ($\bar{1}$08), and ($\bar{3}$08) reflections are on the fourth ring. The ($\bar{3}$28) and ($\bar{1}$28) are on the fifth ring.

10b are merged into one reflection peak around 73°, and the rest of the reflections at other ϕ angles on this ring can be explained similarly as merged reflections. Therefore, the experimental WAXS pattern is also consistent with the predicted $\hat{n}_{45°}$ uniaxial pattern. As one can see in Figure 11c, the eight maxima gradually merge into four maxima with increasing T_c, also

Table 3. Angles between Different Reflections and the $\hat{n}_{45°}$ Axis

d-spacing (nm)	reflections	angle with $\hat{n}_{45°}$ (deg)	reflections	angles with $\hat{n}_{45°}$ (deg)
0.463	$1\bar{2}0$ and $1\bar{2}\bar{0}$	90.0		
(first ring)	$\bar{1}20$ and $1\bar{2}0$	45.0		
0.38−0.40	$\bar{1}32$ and $\bar{2}12$	30.7	$\bar{1}3\bar{2}$ and $\bar{2}1\bar{2}$	149.3
(second ring)	032 and $\bar{2}12$	59.7	$03\bar{2}$ and $\bar{2}1\bar{2}$	120.3
	$11\bar{2}$ and $\bar{1}32$	85.4	$11\bar{2}$ and $\bar{1}3\bar{2}$	94.6
	$11\bar{2}$ and $03\bar{2}$	106.1	$11\bar{2}$ and $03\bar{2}$	73.9
	$\bar{2}04$ and $\bar{1}24$	30.0	$\bar{2}0\bar{4}$ and $\bar{1}2\bar{4}$	150
	$\bar{1}24$ and 004	74.5	$\bar{1}2\bar{4}$ and $00\bar{4}$	105.5
0.33−0.34	$\bar{2}24$	1.6	$\bar{2}2\bar{4}$	178.4
(third ring)	$02\bar{4}$ and $\bar{2}2\bar{4}$	53.0	$02\bar{4}$ and $\bar{2}2\bar{4}$	127
	$0\bar{2}4$	91.6	$0\bar{2}\bar{4}$	88.4
0.25	$\bar{2}44$ and $\bar{3}24$	20.1	$\bar{2}4\bar{4}$ and $\bar{3}2\bar{4}$	159.9
(fourth ring)	044 and $\bar{3}2\bar{4}$	66.5	$04\bar{4}$ and $\bar{3}2\bar{4}$	113.5
	$12\bar{4}$ and $\bar{2}2\bar{4}$	80.1	$12\bar{4}$ and $\bar{2}4\bar{4}$	99.9
	$1\bar{2}4$ and $0\bar{4}4$	102.3	$1\bar{2}\bar{4}$ and $0\bar{4}\bar{4}$	77.7
0.23[a]	$\bar{1}08$	33.1	$\bar{1}0\bar{8}$	146.9
	$\bar{3}08$	70.8	$\bar{3}0\bar{8}$	119.2
0.21−0.22	$\bar{3}\bar{2}8$	17.2	$\bar{3}\bar{2}\bar{8}$	162.8
(fifth ring)	$1\bar{2}8$ and $\bar{3}\bar{2}8$	51.1	$1\bar{2}\bar{8}$ and $\bar{3}\bar{2}\bar{8}$	128.9
	$\bar{1}28$	72.8	$\bar{1}2\bar{8}$	107.2

[a] These reflections are very close to the fourth ring and, therefore, we do not count them as a separate ring.

revealing the increase of the tilt angle away from the $\hat{x}-\hat{y}$ plane with increasing T_c.

It is also important to prove that the experimentally observed 2D WAXS patterns represent a single population of the PEO crystal orientation rather than a mixture of the tilt axis uniaxial pattern and the fiber pattern. We use the 2D WAXS pattern obtained at $T_c = 0$ °C as an example. Note that the first and second rings in the 2D WAXS patterns are superimposed with those in the fiber pattern. Therefore, it is necessary to resort to the orientation of the reflections on the third ring (*d*-spacing of 0.33−0.34 nm), which are found at $\phi = 2°$, 53°, 88°, 92°, 127°, 178°, 182°, 233°, 268°, 272°, 307°, and 358°. Since eight of the reflections at $\phi = 2°$ and 358°, 88° and 92°, 178° and 182°, 268° and 272° are very close, they actually merge into four peaks around $\phi = 0°$, 90°, 180°, and 270°. The azimuthal profiles for these reflections on the third ring at different T_cs are shown in Figure 11d. At $T_c = 0$ °C, there are six maxima at $\phi = 0°$, 64°, 92°, 180°, 268°, and 297°, respectively, of which those at 64° and 297° are much weaker. Another two reflections at $\phi = 127°$ and 233° are overlapped with neighboring reflections due to their relatively weak intensities. The reflections at $\phi = 90°$ and 270° are observed to be stronger compared to those at $\phi = 0°$ and 180°, which may be due to a slight misalignment of the $\hat{n}_{45°}$ around $\hat{z}$. Therefore, the 2D WAXS pattern along $\hat{y}$ at $T_c = 0$ °C is consistent with the $\hat{n}_{45°}$ uniaxial pattern in Figure 10b. If the WAXS pattern in Figure 11a also includes the fiber pattern (Figure 2), there should be reflections at $\phi = 45°$, 135°, 225°, and 315°. Since no discernible reflections are found at those angles, we can conclude that the pattern in Figure 11a is a pure $\hat{n}_{45°}$ uniaxial pattern. Therefore, the *c*-axes of the PEO crystals are preferentially oriented inclined to the $\hat{n}$ direction between $-5 < T_c < 30$ °C.

Based on these analyses, a real-space representation for the crystal orientation between −5 °C $T_c \leq 30$ °C is shown in Figure 12. The crystal *c*-axis is tilted with respect to $\hat{n}$ and randomly

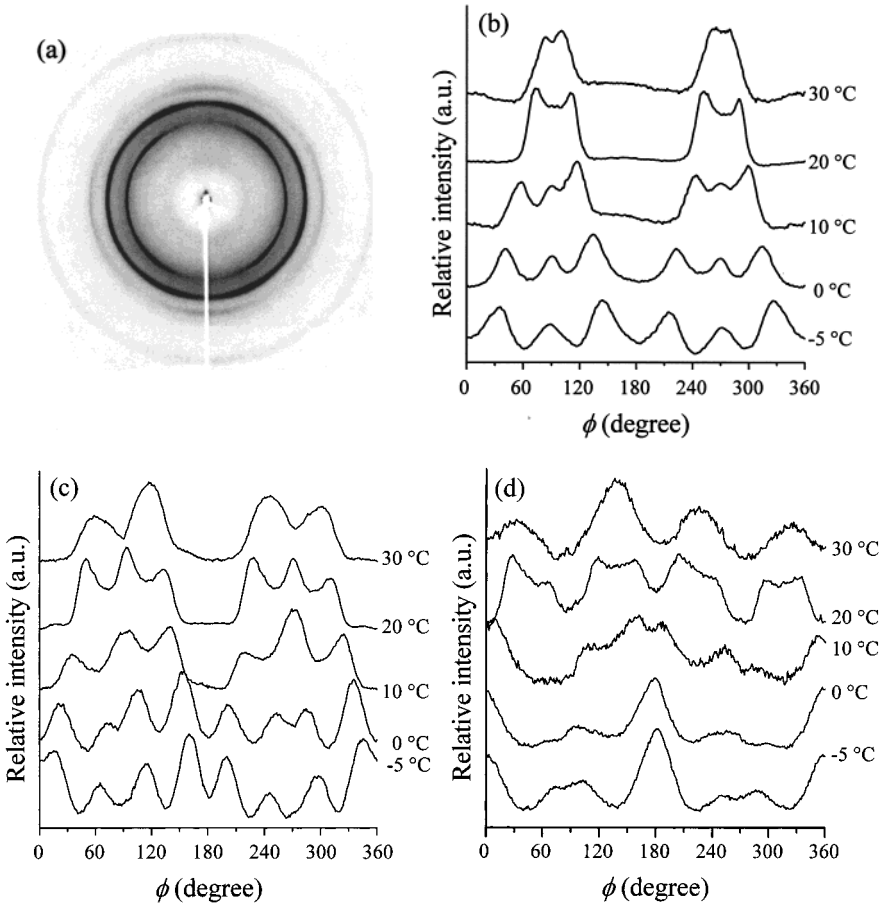

Figure 11. (a) 2D WAXS pattern obtained when the X-ray beam is parallel to $\hat{y}$ at $T_c = 0$ °C. (b) Azimuthal profiles of the (120) reflections on the first ring between $-5 \leq T_c \leq 30$ °C. (c) Azimuthal profiles of the ($\bar{1}32$), (032), ($\bar{2}12$), (112), ($\bar{1}24$), ($\bar{2}04$), and (004) reflections on the second ring between $-5 \leq T_c \leq 30$ °C. (d) Azimuthal profiles of the ($\bar{2}24$) and (024) reflections on the third ring between $-5 \leq T_c \leq 30$ °C.

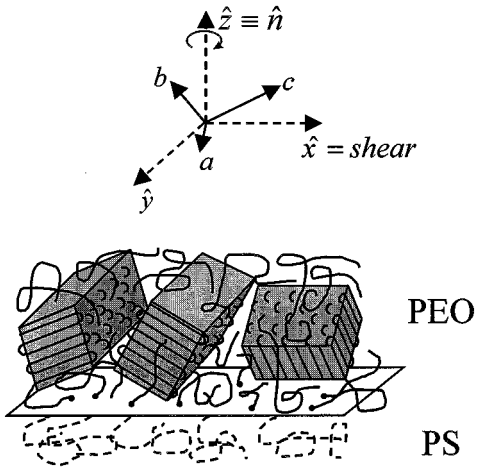

Figure 12. Schematic of an inclined crystal orientation within the confined lamella.

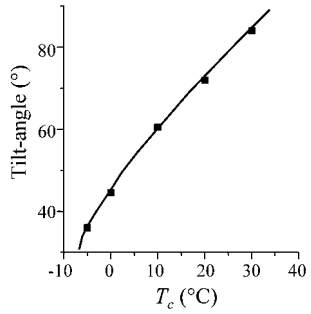

Figure 13. The *c*-axis tilt angle (from the lamellar surface) dependence on T_c.

distributed around $\hat{z}$. From the schematics shown in Figure 12, the left and the middle crystals give rise to the (120) reflections on the quadrants, while the right crystal provides a pair of the (120) reflections in the $\hat{x}-\hat{y}$ plane as the X-ray beam is parallel to $\hat{y}$. With increasing T_c, the four (120) reflections on the quadrant progressively move away from $\hat{z}$ and gradually merge into those reflections in the $\hat{x}-\hat{y}$ plane, indicating an increase of the tilt angle away from the $\hat{x}-\hat{y}$ plane, as shown in Figure 13 (based on the analysis of Figure 11b). An extrapolation to the 90° tilt angle predicts that the crystal *c*-axis will be parallel to $\hat{n}$ at $T_c = 35$ °C.

Crystal Orientation When Isothermally Crystallized above $T_c \geq 35$ °C. 2D SAXS and WAXS patterns along $\hat{y}$ are shown in Figure 14a,b, and 2D SAXS and WAXS along $\hat{z}$ are shown in Figure 14c,d, obtained after the sample is isothermally crystallized at $T_c = 35$ °C. Parts a and c of Figure 14 are the same as previously described, indicating the confined crystallization of the PEO blocks at $T_c = 35$ °C. The 2D WAXS pattern along $\hat{y}$ shows that the (120) reflections are exclusively in the $\hat{x}-\hat{y}$ plane (Figure 14c). This indicates that the *c*-axis of PEO crystals is oriented parallel to $\hat{n}$ ($\hat{z}$). The azimuthal scanning results for different reflections in the 2D WAXS pattern along $\hat{y}$ are shown in Figure 15. On the first ring (*d*-spacing of 0.463 nm), there are two strong maxima at $\phi = 90°$ and 270° for the (120) reflections. On the second ring (*d*-spacing of 0.38−0.40 nm), there are four strong maxima at $\phi = 65°$, 113°, 217°, and 295° for the ($\bar{1}32$), (032), ($\bar{2}12$), and (112) reflections, and four weak maxima at $\phi = 35°$, 144°, 217°, and 324° for the ($\bar{1}24$), ($\bar{2}04$), and (004) reflections. On the third ring (*d*-spacing of 0.33−0.34 nm), there are four maxima at $\phi = 43°$, 134°, 226°, and 316° for the ($\bar{2}24$) and (024) reflections. On the fourth ring (*d*-spacing of 0.25 nm), there are four maxima at $\phi = 56°$, 121°, 238°, and 302° for the (124), ($\bar{3}24$), (044), and ($\bar{2}44$) reflections, and another four maxima at $\phi = 14°$, 165°, 200°, and 343° for the ($\bar{1}08$) and ($\bar{3}08$) reflections. On the fifth ring (*d*-spacing of 0.21−0.22 nm), there are four maxima at $\phi = 31°$, 146°, 209°, and 322° for the ($\bar{3}28$) and ($\bar{1}28$) reflections. These results are consistent with the WAXS fiber pattern in Figure 2 and Table 1, indicating that the 2D WAXS pattern along $\hat{y}$ is actually a PEO crystal fiber pattern.

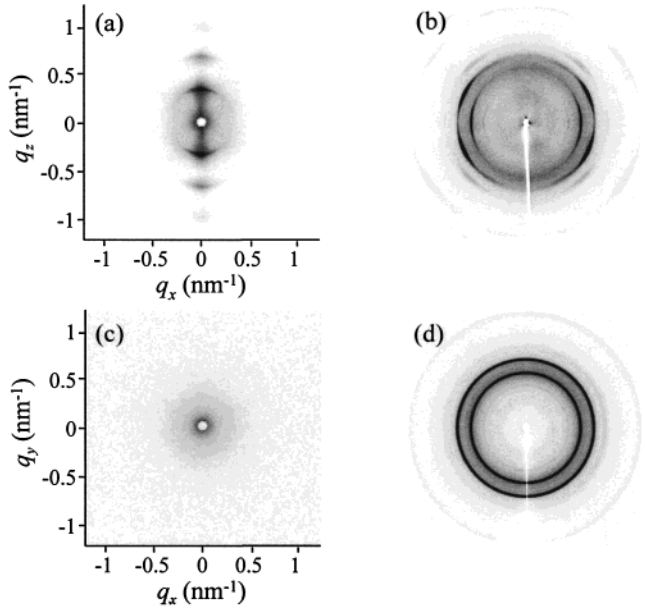

Figure 14. X-ray scattering patterns of the shear-aligned PEO-*b*-PS (8.7K−9.2K) sample isothermally crystallized at $T_c = 35$ °C. (a) 2D SAXS along $\hat{y}$; (b) 2D WAXS along $\hat{y}$; (c) 2D SAXS along $\hat{z}$; and (d) 2D WAXS along $\hat{z}$.

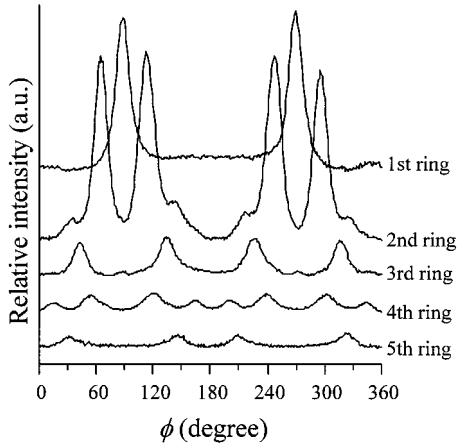

Figure 15. Azimuthal profiles of the (120) reflections on the first ring, the ($\bar{1}32$), (032), ($\bar{2}12$), (112), ($\bar{1}24$), ($\bar{2}04$), and (004) reflections on the second ring, the ($\bar{2}24$) and (024) reflections on the third ring, the (124), ($\bar{3}24$), (044), ($\bar{2}44$), ($\bar{1}08$), and ($\bar{3}08$) reflections on the fourth ring, and the ($\bar{3}28$) and ($\bar{1}28$) on the fifth ring when isothermally crystallized at $T_c = 35$ °C.

The real-space representation of the crystal orientation at $T_c \geq 35$ ° is shown in Figure 16, in which the *c*-axis is parallel to $\hat{n}$. The 2D WAXS along $\hat{z}$ in Figure 14d shows again that the crystal orientation is randomly distributed with respect to $\hat{n}$. Note that if the *c*-axis of PEO crystals is perfectly parallel to $\hat{n}$, then the overlapped reflections on the second and third reflection rings should not appear. However, the experimental 2D WAXS pattern (Figure 14d) still exhibits those reflections (the reflections on the third ring are weak). This can be explained by the

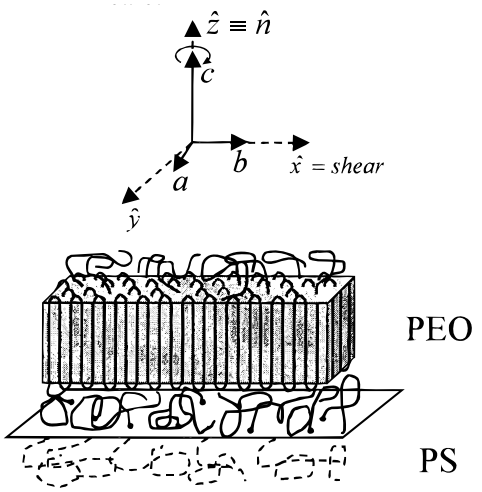

Figure 16. Schematic of a homeotropic crystal orientation within the confined lamella.

misalignment of the crystal orientation and/or the lamellar phase morphology in the sample. From this 2D WAXS pattern, we can estimate the degree of misalignment of the *c*-axis with respect to $\hat{n}$. From Figure 1a, we can calculate that if the *c*-axis rotates $\pm 18°$ around the *b*-axis, the overlapped $(\bar{2}12)$ and (112) reflections will appear (the lower limit). If the *c*-axis rotates $\pm 43°$ around the *b*-axis, the overlapped $(\bar{1}24)$, $(\bar{2}04)$, (004), and $(\bar{1}32)$, (032) reflections will appear (the upper limit). The observation of strong overlapped $(\bar{2}12)$ and $(\bar{1}12)$ reflections and weak overlapped $(\bar{1}32)$, (032), $(\bar{1}24)$, $(\bar{2}04)$, and (004) reflections indicates that the *c*-axis misalignment with respect to $\hat{n}$ should be between 18° and 43°, but close to the lower limit side.

Conclusion

Using combined 2D SAXS and WAXS techniques, nanoconfined crystallization of the PEO blocks between glassy PS layers has been studied on a shear-aligned PEO-*b*-PS diblock copolymer. Crystal orientation (the *c*-axis orientation) with respect to the confined lamellar geometry has been extracted from detailed X-ray diffraction analyses. Four temperature regions have been recognized for different crystal orientations. (1) When the sample is quickly quenched into liquid nitrogen, the *c*-axis in the PEO crystals is randomly oriented. (2) The *c*-axis in the PEO crystals is preferentially oriented perpendicular to $\hat{n}$ (the homogeneous configuration) between $-50 \leq T_c \leq -10$ °C. Upon increasing the T_c from −50 to −10 °C, the crystal orientation gradually improves. (3) The *c*-axis in the PEO crystals is preferentially oriented inclined to $\hat{n}$ between $-5 \leq T_c \leq 30$ °C. Upon increasing the T_c, the tilt angle of the *c*-axis with respect to the lamellar surface gradually increases toward 90°. (4) Finally, the *c*-axis in the PEO crystals is oriented parallel to $\hat{n}$ for $T_c \geq 35$ °C (the homeotropic configuration). This is the first observation that in one diblock copolymer, the crystal orientation between the PS glassy layers changes from random to perpendicular to $\hat{n}$, then to inclined, and finally to parallel to $\hat{n}$ by increasing only T_c. Many interesting aspects regarding nanoconfined crystallization, such as chain-folded lamellar crystal thicknesses and nucleation densities in different T_c regions, and locations of the crystals in confined lamellar space (near the interfaces or in the middle of the lamellae), are subject to further investigations. We are carrying out transmission electron microscopic studies (including bright and dark fields and electron diffraction experiments for thin film samples crystallized at different T_cs) in order to answer these questions. The T_c-dependent crystal orientations are speculated to be critically dependent upon the nucleation density, the lamellar crystal thickness, and the confined lamellar space at different T_cs in addition to the molecular weight of each component in this series of diblock copolymers.

Acknowledgment. This work was supported by NSF (DMR-9617030). The simultaneous SAXS and WAXS experiments were carried out at the National Synchrotron Light Source at Brookhaven National Laboratory.

JA000275E